

# Impact of radio sources and cosmic infrared background on thermal Sunyaev-Zel’dovich - gravitational lensing cross correlation

Masato Shirasaki<sup>1</sup>★

<sup>1</sup>National Astronomical Observatory of Japan, Mitaka, Tokyo 181-8588, Japan

Accepted XXX. Received YYY; in original form ZZZ

## ABSTRACT

Cross correlation with thermal Sunyaev-Zel’dovich (tSZ) effect in cosmic microwave background observation and weak gravitational lensing effect in galaxy imaging survey opens a new window on constraining matter contents in the Universe at redshifts less than 1. In this paper, we study the impact of radio sources and cosmic infrared background (CIB) on observed tSZ-lensing correlation. Assuming the best-fit model of CIB by the *Planck* satellite, we estimate that the residual correlation of CIB with large-scale structures will be of an order of 2% of expected tSZ-lensing correlation from intracluster medium in current lensing surveys. On the other hand, despite large model uncertainties, we find that correlation of lensing and radio sources can induce a *negative* correction for the observed tSZ-lensing correlation with a  $\sim 10 - 30\%$  level. This is originated from positive cross correlation with radio sources and lensing at  $\sim 100$  GHz frequency, whereas tSZ-lensing correlation should show a negative value in temperature fluctuations at that frequency. We also show that the negative correction by radio-lensing correlation can solve the tension between recent measurements of tSZ-lensing correlation and an expected signal from “universal” gas pressure profile of nearby galaxy clusters, when the radio sources with flat-spectral index are assumed to populate massive cluster-sized dark matter halos. Our results indicate that minor source population in radio bands can play an important role in determining observed tSZ-lensing correlation at  $\lesssim 10$  arcmin.

**Key words:** large-scale structure of Universe – methods: analytical – submillimetre: diffuse background

## 1 INTRODUCTION

The observation of cosmic microwave background (CMB) radiation by the *Planck* satellite<sup>1</sup> is among the most crucial for modern astrophysics and cosmology. A wide frequency coverage in the *Planck* observation enables to not only have a robust estimate of CMB (e.g. [Planck Collaboration et al. 2016a](#)), but also study other interesting physical effects printed in CMB radiation. Inverse Compton scattering of CMB photons by hot relativistic electrons ([Zeldovich & Sunyaev 1969](#)), referred to as thermal Sunyaev-Zel’dovich (tSZ) effect, is one of the main science targets in the *Planck* mission (e.g. [Planck Collaboration et al. 2016c](#)). Since the tSZ effect leads to a frequency-dependent distortion of the CMB black-body spectrum ([Zeldovich & Sunyaev 1969](#)), the measurement on different wavelengths is essential as the *Planck* satellite has done. Previous studies have shown that tSZ effect by intracluster medium (ICM) in galaxy clusters is of extreme cosmological importance. The statistics of tSZ effect can probe the abundance of most massive dark matter halos at various redshifts and show a strong dependence on the amplitude

in linear density fluctuations (e.g. [Komatsu & Kitayama 1999](#); [Komatsu & Seljak 2002](#); [Bhattacharya et al. 2012](#)). It is worth noting that the precise measurement of the amplitude in density fluctuations allows us to constrain physics beyond the standard model, including massive neutrinos (e.g. [Saito et al. 2008](#)), dark matter (e.g. [Smith & Markovic 2011](#); [Enqvist et al. 2015](#)), and cosmic acceleration (e.g. [Weinberg et al. 2013](#)).

To use tSZ effect for cosmological analyses, we need accurate modeling of ICM. The tSZ statistics have degeneracy between the ICM property and cosmological parameters in principle (e.g. [Battaglia et al. 2010](#)). Hence, the current cosmological constraints by the tSZ statistics hinge on the still poorly understood property of ICM (e.g. [Planck Collaboration et al. 2016c](#); [Horowitz & Seljak 2017](#)). Various approaches have been proposed to learn the ICM physics more and break the degeneracy in tSZ statistics with astronomical measurements other than tSZ effect (e.g. [Battaglia et al. 2017](#); [Hill et al. 2018](#)). Among them, the measurement of gravitational lensing effect in galaxy imaging survey can play a central role in determining the relation between the ICM and large-scale structures.

Gravitational lensing effect causes a small distortion in shape of distant sources and its amplitude depends on surface mass density

★ E-mail: masato.shirasaki@nao.ac.jp

<sup>1</sup> <https://www.cosmos.esa.int/web/planck>

in the direction of individual sources (e.g. Bartelmann & Schneider 2001, for review). Therefore, the information of total matter density (including dark matter) can be obtained with the lensing measurement, and those information would be a base for developing accurate model of ICM. Battaglia et al. (2015) have shown that the cross correlation between tSZ and lensing can probe the ICM over a wide range of halo masses and redshifts and future measurement of the cross correlation can constrain the relation between ICM and dark matter halos with a 5-20% precision.

Recently, the measurements of tSZ-lensing cross correlation have been performed with lensing data in the Canada France Hawaii Lensing Survey<sup>2</sup> (CFHTLenS: Van Waerbeke et al. 2014) and the Red Cluster Sequence Lensing Survey<sup>3</sup> (RCSLenS: Hojjati et al. 2017). The signal-to-noise ratio in the latest measurement already reaches a  $13 - 17\sigma$  level (Hojjati et al. 2017), implying that ongoing and future lensing surveys will be able to present more precise measurements. A natural question then arises: can we explain the observed tSZ-lensing correlation in CFHTLenS and RCSLenS assuming the ICM properties observed in nearby clusters (e.g. Planck Collaboration et al. 2013)? This question is still under debate. At least, it seems difficult to explain the tSZ-lensing correlation at angular scale of  $< 10$  arcmin by the model with the ICM property from local observation (Ma et al. 2015). To fill the gap, one may need a relatively small amplitude in matter density fluctuations today compared to the constraint by CMB measurements and/or a strong baryonic feedback by active galactic nuclei (AGN) in galaxy groups (Hojjati et al. 2017). Furthermore, Osato et al. (2018) examined a semi-analytic model of ICM in Shaw et al. (2010) to explain both of the tSZ-lensing correlation in Hojjati et al. (2017) and the power spectrum of tSZ effect measured in Planck Collaboration et al. (2016c). The authors found that the tSZ power spectrum prefers  $\sim 30\%$  of ICM pressure at outer region in galaxy clusters to be non-thermal, while the tSZ-lensing correlation prefers a much lower fraction of non-thermal pressure with a level of  $\lesssim 5\%$ . At present, the ICM model in Shaw et al. (2010) cannot explain the both statistics simultaneously without reducing gas fraction in group-scaled halos.

Motivated by the inconsistency between the observed tSZ-lensing signal and the model with the ICM property of nearby clusters constrained by Planck (Planck Collaboration et al. 2013), we here consider other relevant effects in the cross correlation measurement. In this paper, we study the impact of the presence of astrophysical sources in brightness temperature maps on the cross correlation measurement. Except for galactic sources, relevant sources in the cross correlation measurement are expected to be radio point sources and cumulative emission from star-forming dusty galaxies, referred to as cosmic infrared backgrounds (CIB). The impact of those extragalactic sources on construction of tSZ map has been studied in Planck Collaboration et al. (2014b) and Planck Collaboration et al. (2016c), while it still remains uncertain if one can ignore the radio sources and CIB in the tSZ-lensing cross correlation (see Hurier 2015, for the study with a similar motivation). We work with a simple halo-model approach to predict possible contamination in the tSZ-lensing correlation induced by relevant astrophysical sources living in large-scale structures at various redshifts. Using our model, we evaluate the corrections for the observed tSZ-lensing correlation signal by CIB- and radio-lensing correlations.

This paper is organized as follows. In Section 2, we first de-

scribe the methodology for construction of tSZ effect from multiple-frequency CMB measurements and discuss the possible effects from astrophysical sources at frequency bands of interest. We then summarize the basics of gravitational lensing and the cross correlation between tSZ and lensing in Section 3. Our model of the tSZ-lensing correlation is summarized in Section 4 and Section 5 presents the outcome of our model and comparison of the observed tSZ-lensing correlation with the model. We conclude the paper in Section 6. Throughout this study, we adopt the flat-geometry  $\Lambda$ CDM (Lambda cold dark matter) model that is consistent with the Planck 2015 results (see the result of “TT+lowP+lensing” in Planck Collaboration et al. 2016b). The cosmological parameters are as follows: the matter density,  $\Omega_{m0} = 1 - \Omega_{\Lambda} = 0.308$ , the baryon density,  $\Omega_{b0} = 0.0484$ , the Hubble parameter,  $h = H_0/(100\text{km s}^{-1}\text{Mpc}^{-1}) = 0.678$ , the present amplitude of density contrast at  $8 h^{-1}\text{Mpc}$ ,  $\sigma_8 = 0.8149$ , and the spectral index,  $n_s = 0.9677$ .

## 2 ESTIMATION OF TSZ EFFECT FROM CMB MEASUREMENTS

At frequency  $\nu$ , the change in CMB temperature by the tSZ effect is expressed as

$$\frac{\Delta T}{T_0} = g(x)y, \quad (1)$$

where  $T_0 = 2.725\text{K}$  is the CMB temperature (Fixsen 2009),  $g(x) = x\coth(x/2) - 4$  with  $x = h\nu/k_B T_0$ ,  $h$  and  $k_B$  are the Planck constant and the Boltzmann constant, respectively<sup>4</sup>. Compton parameter  $y$  is computed as the integral of the electron pressure  $P_e$  along a line of sight:

$$y(\theta) = \int_0^{\chi_H} \frac{d\chi}{1+z} \frac{k_B \sigma_T}{m_e c^2} P_e(r(\chi)\theta, z(\chi)), \quad (2)$$

where  $\sigma_T$  is the Thomson cross section,  $\chi$  is the comoving radial distance to redshift  $z$ ,  $r(\chi)$  is the angular diameter distance, and  $\chi_H$  is the comoving distance up to  $z \rightarrow \infty$ .

Given the frequency dependence in the tSZ effect as Eq. (1), one can construct an estimator of Compton  $y$  map from brightness temperature maps at multiple frequencies as

$$\hat{y}(\theta) = \sum_i w_i \frac{T_i(\theta)}{T_0}, \quad (3)$$

where  $\hat{y}$  is an estimated Compton  $y$  parameter,  $T_i$  is the observed temperature at  $i$ -th frequency  $\nu_i$  and the sum in Eq. (3) is over frequency bands of interest. Van Waerbeke et al. (2014) imposed three conditions to construct the Compton  $y$  map for the cross correlation with the tSZ effect and weak lensing effect in galaxy shapes. Those include (i)  $\sum_i g(x_i)w_i = 1$  to produce an unbiased Compton  $y$  map on average, (ii)  $\sum_i w_i = 0$  to null the primary CMB fluctuations, and (iii)  $\sum_i w_i \cdot c_i \nu_i^{\beta_d} = 0$  to remove a contribution from dust emission with spectral index  $\beta_d \sim 2$  in antenna temperature units (The factor  $c_i$  is given by the conversion of antenna temperature to thermodynamic temperature. See also Section 4.2). In Van Waerbeke et al. (2014), the authors worked on the Planck temperature maps (Planck Collaboration et al. 2014a) at four frequency bands of 100,

<sup>4</sup> In this paper, we ignore the relativistic correction for  $g(x)$  which is only important for the tSZ effects in most massive galaxy clusters (Itoh et al. 1998; Nozawa et al. 1998). Note that the tSZ-lensing correlation can probe the ICM at clusters with masses of  $\sim 10^{14} h^{-1} M_{\odot}$  (Ma et al. 2015; Osato et al. 2018).

<sup>2</sup> <http://www.cfhtlens.org/>

<sup>3</sup> <http://www.rcslens.org/>

143, 217, and 353 GHz to determine the weight  $w_i$  for different  $\beta_d$ . Throughout this paper, we work with the weight in the  $y$  map named *Planck C* in Van Waerbeke et al. (2014) for representative example.

In addition to estimating the tSZ effect, Van Waerbeke et al. (2014) examined to set different weights in Eq. (3) by projecting out the both of tSZ effect and primary CMB fluctuation (i.e.  $\sum_i g(x_i)w_i = \sum_i w_i = 0$ ). Even after nulling the tSZ effect in Eq. (3), they found a weak correlation of the observed  $\hat{y}$  and weak lensing (see Figure 4 in Van Waerbeke et al. (2014)). This supports that the contamination in  $y$  map construction should (partly) arise from some extragalactic sources since weak gravitational lensing effect is relevant for the large-scale structures at  $z \sim 0.2 - 0.4$  (Van Waerbeke et al. 2013, also see Figure 1). In this paper, we study the correlation of  $\hat{y}$  and gravitational lensing when setting weight in Eq. (3) so as to remove the tSZ effect<sup>5</sup>. For the weight so as to null the tSZ effect in  $\hat{y}$  map, we work with the case named as *Planck E'* in Van Waerbeke et al. (2014).

Note that the *Planck* team has worked on more sophisticated approach than Eq. (3) to construct a Compton  $y$  map. They allowed a spatially varying weight in Eq. (3) (see Planck Collaboration et al. 2016c, for the latest map). For a spatially varying weight, we can easily take into account the effect on the cross correlation measurements by using the formula in the Appendix A of Planck Collaboration et al. (2014b). The primary purpose in this paper is to follow the analyses in Van Waerbeke et al. (2014), and we leave it to future work to include the effect of spatially varying weight.

Nevertheless, the following results are expected to be less affected by the choice of the weight in Eq. (3) or spatially varying weight in Planck Collaboration et al. (2016c). First of all, the spatially varying weights can reduce the contamination from spatially-resolved objects (Hurier et al. 2013), but it is no longer valid for unresolved sources such as CIB or faint radio sources. Also, the spatially varying weight in Planck Collaboration et al. (2016c) is introduced so as to localize tSZ effects in temperature maps at different frequency channels. Hence, the frequency dependence of such weight is expected to be similar to one of the weight in Eq. (3). In addition, the weight in Planck Collaboration et al. (2016c) uses small-scale information of temperature maps to localize the tSZ effects, leaving the impact of faint localized objects on the cross correlation analysis.

### 3 CROSS CORRELATION WITH COMPTON Y AND WEAK LENSING

As introduced in Section 2, the actual observable  $\hat{y}$  is given by the linear combination of brightness temperature as in Eq. (3). Here we summarize the basic of the cross correlation between  $\hat{y}$  map and weak gravitational lensing effect in galaxy imaging survey. Lensing convergence  $\kappa$  is responsible for the strength of weak gravitational lensing effect. Under the Born approximation, one can express the lensing convergence field as the weighted integral of matter overdensity field  $\delta_m(\mathbf{x})$  (Bartelmann & Schneider 2001):

$$\kappa(\boldsymbol{\theta}) = \int_0^{\chi_H} d\chi W_\kappa(\chi) \delta_m(r(\chi)\boldsymbol{\theta}, z(\chi)), \quad (4)$$

<sup>5</sup> The conditions in Van Waerbeke et al. (2014) for nulling tSZ cannot determine the overall normalization of weights. This degree of freedom does not affect our results since we use the same weights as in Van Waerbeke et al. (2014).

where  $W_\kappa(\chi)$  is called lensing kernel. For a given redshift distribution of source galaxies, the lensing kernel is expressed as

$$W_\kappa(\chi) = \frac{3}{2} \left( \frac{H_0}{c} \right)^2 \Omega_{m0} \frac{r(\chi)}{a(\chi)} \int_\chi^{\chi_H} d\chi' p(\chi') \frac{r(\chi' - \chi)}{r(\chi')}, \quad (5)$$

where  $p(\chi)$  represents the redshift distribution of source galaxies normalized to  $\int d\chi p(\chi) = 1$ . Hence, the quantity of interest in this paper is defined as

$$\xi_{y-\kappa}(\boldsymbol{\theta}) \equiv \langle \hat{y}(\boldsymbol{\phi}) \kappa(\boldsymbol{\phi} + \boldsymbol{\theta}) \rangle = \sum_i w_i / T_0 \langle T_i(\boldsymbol{\phi}) \kappa(\boldsymbol{\phi} + \boldsymbol{\theta}) \rangle, \quad (6)$$

and the cross correlation of  $\xi_{y-\kappa}$  can be computed as (e.g. Hojjati et al. 2017)

$$\xi_{y-\kappa}(\boldsymbol{\theta}) = \sum_\ell \left( \frac{2\ell + 1}{4\pi} \right) C_{y-\kappa}(\ell) P_\ell(\cos \theta) b_\ell^\kappa b_\ell^y, \quad (7)$$

where  $P_\ell$  are the Legendre polynomials,  $b_\ell^\kappa$  and  $b_\ell^y$  are the smoothing kernel of  $\kappa$  and  $\hat{y}$  maps, respectively. The power spectrum of  $C_{y-\kappa}(\ell)$  can be decomposed into

$$C_{y-\kappa}(\ell) = \left( \sum_i w_i g(x_i) \right) C_{y-\kappa}(\text{tSZ}|\ell) + \sum_i w_i C_{\kappa-T}(\nu_i|\ell), \quad (8)$$

where the first term in the right hand side expresses the correlation of tSZ effect and lensing convergence as studied in the literature, whereas the second term is new contribution arising from the correlation of astrophysical sources in the *Planck* bands and lensing convergence. Note that the second term in the r.h.s of Eq. (8) can have different dependence in frequency  $\nu$  from tSZ effect and CMB black-body spectrum, and it cannot be vanished in general. We define  $C_{\kappa-T}(\nu_i|\ell)$  to be dimensionless by normalizing the  $T$  field with CMB temperature  $T_0$  throughout this paper.

## 4 MODEL

In this section, we describe a theoretical model of Eq. (8) based on halo-model approach.

### 4.1 Intracluster medium

We first summarize the halo-model prediction of tSZ-lensing cross correlation induced by ICM as developed in Hill & Spergel (2014); Ma et al. (2015). In the halo model, we can decompose the power spectrum into two components as:

$$C_{y-\kappa} = C_{y-\kappa}^{1h} + C_{y-\kappa}^{2h}, \quad (9)$$

where the first term in the r.h.s arises from the correlation within single halos, while the second term represents the correlation due to clustering of neighboring halos. For tSZ effect, one can express those terms as

$$C_{y-\kappa}^{1h}(\text{tSZ}|\ell) = \int_0^{z_{\max}} dz \frac{dV}{dzd\Omega} \int_{M_{\min}}^{M_{\max}} dM \frac{dn}{dM} y_\ell(M, z) \kappa_\ell(M, z), \quad (10)$$

$$C_{y-\kappa}^{2h}(\text{tSZ}|\ell) = \int_0^{z_{\max}} dz \frac{dV}{dzd\Omega} P_L(k = \ell/\chi, z) \times \left[ \int_{M_{\min}}^{M_{\max}} dM \frac{dn}{dM} y_\ell(M, z) b(M, z) \right] \times \left[ \int_{M_{\min}}^{M_{\max}} dM \frac{dn}{dM} \kappa_\ell(M, z) b(M, z) \right], \quad (11)$$

where we set  $z_{\max} = 7$ ,  $M_{\min} = 10^{10} h^{-1} M_{\odot}$  and  $M_{\max} = 10^{16} h^{-1} M_{\odot}$ ,  $P_L(k, z)$  is the linear matter power spectrum,  $dn/dM$  is the halo mass function, and  $b$  is the linear halo bias. In this paper, we define the halo mass  $M$  by spherical overdensity (SO) with respect to 200 times mean matter density. We adopt the model of halo mass function in [Tinker et al. \(2008\)](#) and linear bias in [Tinker et al. \(2010\)](#). In Eqs. (10) and (11),  $\kappa_{\ell}$  is the Fourier transform of lensing convergence profile of single dark matter halo with the NFW density profile ([Navarro et al. 1996](#)):

$$\kappa_{\ell}(M, z) = \frac{W_{\kappa}(\chi(z))}{\chi^2} \int dr 4\pi r^2 \frac{\sin(\ell r/\chi)}{\ell r/\chi} \frac{\rho_{\text{NFW}}(r, M, z)}{\bar{\rho}_m}, \quad (12)$$

where  $\rho_{\text{NFW}}$  is the NFW profile and  $\bar{\rho}_m$  is the mean matter density in the Universe. The NFW profile can be characterized by single parameter called halo concentration for a given SO mass. In this paper, we adopt the model of halo concentration developed in [Diemer & Kravtsov \(2015\)](#).

Similarly, we define  $y_{\ell}$  in Eqs. (10) and (11) as the Fourier transform of Compton  $y$  profile in single halo (see Eq. 2):

$$y_{\ell}(M, z) = \frac{4\pi r_{500}}{\ell_{500}^2} \frac{\sigma_T}{m_e c^2} \int dx x^2 \frac{\sin(\ell x/\ell_{500})}{\ell x/\ell_{500}} P_{e,h}(x, M, z), \quad (13)$$

where  $r_{500}$  is the SO radius with respect to 500 times critical density, we define as  $x = ar/r_{500}$  and  $\ell_{500} = a\chi/r_{500}$ . When computing  $y_{\ell}$ , we adopt the model of 3D electron pressure profile in single halo  $P_{e,h}$  as constrained in [Planck Collaboration et al. \(2013\)](#),

$$P_{e,h}(x = r/r_{500}, M, z) = 1.65 \times 10^{-3} \left[ \text{keV cm}^{-3} \right] E^{8/3}(z) \times \left( \frac{M_{500}}{3 \times 10^{14} h_{70}^{-1} M_{\odot}} \right)^{2/3+0.12} P(x) h_{70}^2, \quad (14)$$

where  $E(z) = H(z)/H_0$ ,  $h_{70} = H_0/70$ ,  $M_{500} = 4/3\pi \cdot 500 \rho_{\text{crit}} r_{500}^3$  ( $\rho_{\text{crit}}$  is the critical density in the Universe) and  $P(x)$  is so-called universal pressure profile ([Nagai et al. 2007](#)). The functional form of  $P(x)$  is given by

$$P(x) = \frac{P_0}{(c_{500}x)^{\gamma} [1 + (c_{500}x)^{\alpha}]^{(\beta-\gamma)/\alpha}}, \quad (15)$$

where we adopt the best-fit values of five parameters ( $P_0$ ,  $c_{500}$ ,  $\alpha$ ,  $\beta$ , and  $\gamma$ ) from [Planck Collaboration et al. \(2013\)](#). Note that the input mass parameter  $M_{500}$  in Eq. (14) will be affected by hydrostatic mass bias. For a given halo mass of  $M$  (the SO mass w.r.t 200 times mean matter density), we compute  $M_{500}$  by using the halo concentration as in [Hu & Kravtsov \(2003\)](#) and then include the hydrostatic mass bias  $b_{\text{HM}}$  by  $M_{500} \rightarrow (1 - b_{\text{HM}})M_{500}$  and  $r_{500} \rightarrow (1 - b_{\text{HM}})^{1/3}r_{500}$  for Eq. (14). We set  $1 - b_{\text{HM}} = 0.833$  as follows in [Dolag et al. \(2016\)](#).

It is worth noting that [Dolag et al. \(2016\)](#) have shown the above ICM model can explain the observed tSZ power spectrum ([Planck Collaboration et al. 2016c](#)). In fact, one can also explain the tSZ-lensing correlations ([Van Waerbeke et al. 2014](#); [Hojjati et al. 2017](#)) with the above ICM model by setting  $P_0 \sim 4.4$  (the best-fit value from *Planck* analysis is 6.41), whereas it turns to be difficult to explain the tSZ power spectrum. In addition, the value of  $P_0 \sim 4.4$  is inconsistent with the observations of nearby galaxy clusters ([Arnaud et al. 2010](#); [Planck Collaboration et al. 2013](#)).

## 4.2 Astrophysical sources

Next we consider cumulative emission from astrophysical sources at frequency of 100 – 800 GHz and the cross correlation with lensing

convergence field. At the frequency of interest, relevant astrophysical sources include point sources in radio bands, referred to as radio galaxies or/and radio AGN in the literature, and CIB emission.

Observed specific intensity at a given frequency  $\nu$  can be expressed as

$$I_{\nu}(\theta) = \int \frac{d\chi}{1+z} j_{\nu}(r(\chi)\theta, z(\chi)), \quad (16)$$

where  $j_{\nu}(x)$  represents the comoving specific emission coefficient. One can convert the specific intensity to antenna temperature using the CMB black-body spectrum as

$$T_{\nu}(\theta) = \left( \frac{\partial B_{\nu}}{\partial T} \Big|_{T=T_0} \right)^{-1} I_{\nu}(\theta), \quad (17)$$

$$\frac{\partial B_{\nu}}{\partial T} \Big|_{T=T_0} = 99.27 \left[ \text{Jy str}^{-1} / \mu\text{K} \right] \frac{x^4 e^x}{(e^x - 1)^2}, \quad (18)$$

where  $x = h\nu/k_{\text{B}}T_0 = \nu/56.84 \text{ GHz}$ .

In the halo-model approach, we can relate the emission coefficient with underlying astrophysical sources as follows (e.g. [Shang et al. 2012](#)):

$$j_{\nu} = \int dL \frac{dn}{dL}(L, z) \frac{L_{(1+z)\nu}}{4\pi}, \quad (19)$$

where  $L$  is the luminosity in infrared or radio for our case,  $dn/dL$  represents the luminosity function, and  $L_{(1+z)\nu}$  is related to the flux  $S_{\nu}$  from relevant object as

$$S_{\nu} = \frac{(1+z)^{-1} L_{(1+z)\nu}}{4\pi \chi^2}. \quad (20)$$

In the Appendix, we summarize the derivation for cross power spectra of weak lensing and astrophysical sources based on the halo model.

### Radio sources

For radio sources, we work with three-population model as introduced in [de Zotti et al. \(2005\)](#). In this model, extragalactic radio sources consist of flat-spectrum radio quasars (FSRQs), BL Lac objects, and steep-spectrum sources. Their spectral index is assumed to be  $\alpha = 0.1$ ,  $0.1$ , and  $0.7$  for FSRQs, BL Lac objects, and steep-spectrum sources, respectively (the index is defined in terms of  $S_{\nu} \propto \nu^{-\alpha}$ ). The radio luminosity function at 1.4 GHz for these three populations has been constrained in [Massardi et al. \(2010\)](#) with local luminosity functions, multifrequency source counts and redshift distributions. In this paper, we adopt the radio luminosity function in [Massardi et al. \(2010\)](#) and assume that the emission coefficient from extragalactic radio sources can be computed as

$$j_{\nu} \simeq \sum_i \int dL_{1.4} \frac{dn_i}{dL_{1.4}} \frac{L_{(1+z)\nu,i}(L_{1.4})}{4\pi} (1 + \delta_i), \quad (21)$$

$$L_{(1+z)\nu,i} = \frac{L_{1.4}}{(1+z)^2} \left[ \frac{(1+z)\nu}{1.4 \text{ GHz}} \right]^{-\alpha_i}, \quad (22)$$

where  $L_{1.4}$  is the radio luminosity at 1.4 GHz, and the index of  $i$  runs over BL Lac objects and steep-spectrum sources<sup>6</sup>. In Eq. (21),  $\delta_i$  represents the fluctuation in number density of radio sources. In

<sup>6</sup> We ignore the contributions from FSRQs in the following, since the FSRQs will have much smaller number density than other two sources at the relevant redshift of  $\lesssim 1$ .



this paper, we predict the term of  $\delta_i$  by using the following halo-occupation distribution (HOD):

$$\delta_i(\mathbf{x}, M) \propto \exp\left(-\frac{M_{\text{cut},i}}{M}\right) \delta_{\text{D}}^{(3)}(\mathbf{x}), \quad (23)$$

where  $\delta_{\text{D}}^{(n)}$  is the  $n$ -dimensional Dirac delta function and we assume all the radio sources locate at the center of their host halo. The functional form of HOD is motivated by the study in Wake et al. (2008). For steep-spectrum radio sources, we adopt the best-fit value of  $M_{\text{cut}} = 9.65 \times 10^{13} h^{-1} M_{\odot}$  from Wake et al. (2008), whereas we examine various values of  $M_{\text{cut}}$  for BL Lac objects. Note that the steep-spectrum sources dominate the observed flux counts at  $\sim$ GHz frequency in this model (Massardi et al. 2010). This indicates that the clustering measurements of radio sources in the literature should be mainly determined by the clustering of steep-spectrum sources within our framework, allowing us to vary the typical host halo mass for BL Lac objects.

Given the model as above, we can compute the cross power spectrum of radio sources and lensing convergence as

$$C_{\kappa-T}^{\text{R}}(\nu|\ell) = C_{\kappa-T}^{\text{R,1h}}(\nu|\ell) + C_{\kappa-T}^{\text{R,2h}}(\nu|\ell), \quad (24)$$

$$\begin{aligned} C_{\kappa-T}^{\text{R,1h}}(\nu|\ell) &= \sum_i \int_0^{\chi_H} \frac{d\chi}{\chi^2} W_{\text{R},i}(\chi) W_{\kappa}(\chi) \bar{\rho}_{\text{m}}^{-1} \\ &\times \left[ \int_{M_{\text{min}}}^{M_{\text{max}}} dM \frac{dn}{dM} \exp\left(-\frac{M_{\text{cut},i}}{M}\right) \tilde{\rho}_{\text{NFW}}(k = \ell/\chi, M, z) \right] \\ &\times \left[ \int_{M_{\text{min}}}^{M_{\text{max}}} dM \frac{dn}{dM} \exp\left(-\frac{M_{\text{cut},i}}{M}\right) \right]^{-1}, \quad (25) \end{aligned}$$

$$\begin{aligned} C_{\kappa-T}^{\text{R,2h}}(\nu|\ell) &= \sum_i \int_0^{\chi_H} \frac{d\chi}{\chi^2} W_{\text{R},i}(\chi) W_{\kappa}(\chi) \bar{\rho}_{\text{m}}^{-1} P_{\text{L}}(k = \ell/\chi, z) \\ &\times \left[ \int_{M_{\text{min}}}^{M_{\text{max}}} dM \frac{dn}{dM} \tilde{\rho}_{\text{NFW}}(k = \ell/\chi, M, z) b(M, z) \right] \\ &\times \left[ \int_{M_{\text{min}}}^{M_{\text{max}}} dM \frac{dn}{dM} \exp\left(-\frac{M_{\text{cut},i}}{M}\right) b(M, z) \right] \\ &\times \left[ \int_{M_{\text{min}}}^{M_{\text{max}}} dM \frac{dn}{dM} \exp\left(-\frac{M_{\text{cut},i}}{M}\right) \right]^{-1}, \quad (26) \end{aligned}$$

where  $\tilde{\rho}_{\text{NFW}}$  is the Fourier transform of NFW profile and the effective window in radio  $W_{\text{R},i}$  is defined as

$$\begin{aligned} W_{\text{R},i}(\chi(z)) &= \frac{1}{T_0} \left( \frac{\partial B_{\nu}}{\partial T} \Big|_{T=T_0} \right)^{-1} \\ &\times \frac{1}{1+z} \int_{L_{\text{min}}}^{L_{\text{max}}} dL_{1.4} \frac{dn_i}{dL_{1.4}} \frac{L_{(1+z)\nu,i}(L_{1.4})}{4\pi}, \quad (27) \end{aligned}$$

where we set  $L_{\text{min}} = 10^{30} \text{ erg s}^{-1} \text{ Hz}^{-1}$  and  $L_{\text{max}} = 10^{50} \text{ erg s}^{-1} \text{ Hz}^{-1}$ .

### Cosmic Infrared Background

For CIB, we follow the model developed in Shang et al. (2012). In this model, Eq. (19) is rewritten as

$$\begin{aligned} j_{\nu} &= \int dM \frac{dn}{dM} \frac{1}{4\pi} \left[ N_{\text{cen}} L_{(1+z)\nu, \text{cen}}(M, z) \right. \\ &\quad \left. + \int dm \frac{dn_{\text{sub}}}{dm}(m, M, z) L_{(1+z)\nu, \text{sat}}(m, z) \right], \quad (28) \end{aligned}$$

$$\equiv \int dM \frac{dn}{dM} [f_{\nu, \text{cen}}(M, z) + f_{\nu, \text{sat}}(M, z)], \quad (29)$$

where  $N_{\text{cen}}$  is the HOD of central galaxies,  $L$  is the infrared luminosity,  $m$  is the subhalo mass, and  $dn_{\text{sub}}/dm$  is the subhalo mass function. In this paper, we use the model of subhalo mass function in Tinker & Wetzel (2010). As seen in Eq. (28), the model assumes the statistical relation between the luminosity  $L$  and (sub)halo mass and terms of  $L_{(1+z)\nu}$  are responsible for the  $L - M$  relation. For simplicity, we assume there are no differences of the  $L - M$  relation between halos and subhalos, i.e.  $L_{(1+z)\nu, \text{cen}} = L_{(1+z)\nu, \text{sat}}$ . The functional form of  $L_{(1+z)\nu}$  is characterized with seven physical parameters. We also assume  $N_{\text{cen}} = 1$  for  $M > M_{\text{cen}}$  and 0 otherwise. We adopt the best-fit parameters in the  $L - M$  relation and the value of  $M_{\text{cen}}$  to the recent CIB measurement by the *Planck* satellite (Planck Collaboration et al. 2014d).

Hence, we can express the cross power spectrum between CIB and lensing convergence as

$$C_{\kappa-T}^{\text{CIB}}(\nu|\ell) = C_{\kappa-T}^{\text{CIB,1h}}(\nu|\ell) + C_{\kappa-T}^{\text{CIB,2h}}(\nu|\ell), \quad (30)$$

$$\begin{aligned} C_{\kappa-T}^{\text{CIB,1h}}(\nu|\ell) &= \int_0^{\chi_H} \frac{d\chi}{\chi^2} W_{\text{CIB}}(\chi) W_{\kappa}(\chi) \bar{\rho}_{\text{m}}^{-1} \\ &\times \int_{M_{\text{min}}}^{M_{\text{max}}} dM \frac{dn}{dM} \left[ f_{\nu, \text{cen}}(M, z) \right. \\ &\quad \left. + f_{\nu, \text{sat}}(M, z) \tilde{u}_{\text{sat}}(k = \ell/\chi, M, z) \right] \tilde{\rho}_{\text{NFW}}(k = \ell/\chi, M, z), \quad (31) \end{aligned}$$

$$\begin{aligned} C_{\kappa-T}^{\text{CIB,2h}}(\nu|\ell) &= \int_0^{\chi_H} \frac{d\chi}{\chi^2} W_{\text{CIB}}(\chi) W_{\kappa}(\chi) \bar{\rho}_{\text{m}}^{-1} P_{\text{L}}(k = \ell/\chi, z) \\ &\times \left[ \int_{M_{\text{min}}}^{M_{\text{max}}} dM \frac{dn}{dM} \tilde{\rho}_{\text{NFW}}(k = \ell/\chi, M, z) b(M, z) \right] \\ &\times \left[ \int_{M_{\text{min}}}^{M_{\text{max}}} dM \frac{dn}{dM} \left( f_{\nu, \text{cen}}(M, z) \right. \right. \\ &\quad \left. \left. + f_{\nu, \text{sat}}(M, z) \tilde{u}_{\text{sat}}(k = \ell/\chi, M, z) \right) b(M, z) \right], \quad (32) \end{aligned}$$

where  $u_{\text{sat}}(\mathbf{x})$  is the number density profile of satellite galaxies normalized to  $\int u_{\text{sat}} dV = 1$ , and  $\tilde{u}_{\text{sat}}$  is the Fourier counterpart. We assume  $u_{\text{sat}} = \rho_{\text{NFW}}/M$  throughout this paper. The kernel function of  $W_{\text{CIB}}(\chi)$  is given by

$$W_{\text{CIB}}(\chi(z)) = \frac{1}{T_0} \left( \frac{\partial B_{\nu}}{\partial T} \Big|_{T=T_0} \right)^{-1} \frac{1}{1+z}. \quad (33)$$

### 4.3 Effective redshifts in cross correlations of astrophysical sources and lensing

Before detailed computations, we shall show the effective redshift range to be probed by the cross correlation between astrophysical

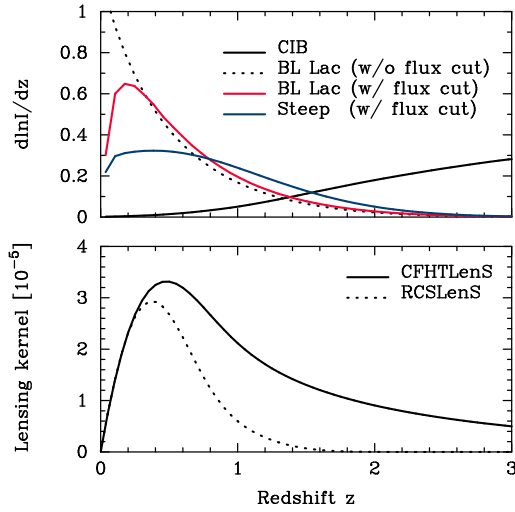


**Figure 1.** *Top:* Redshift dependence of mean intensity from cosmic infrared background (CIB) and cumulative radio sources. We show the CIB intensity at 217 GHz and radio intensity at 100 GHz. *Bottom:* The lensing efficiency in current lensing surveys.

sources at millimeter wavelengths and lensing convergence. For this purpose, we compute the mean intensity from cumulative emission from radio sources and CIB. For  $i$ -th radio source (BL Lac object or steep-spectrum source), the mean intensity is given by

$$I_{\nu,i}^R = \int_0^{\chi_H} \frac{d\chi}{1+z} \int_{L_{\min}}^{L_{\max}} dL_{1.4} \frac{dn_i}{dL_{1.4}} \frac{L_{(1+z)\nu,i}(L_{1.4})}{4\pi}, \quad (34)$$

while the CIB mean intensity can be computed as

$$I_{\nu}^{\text{CIB}} = \int_0^{\chi_H} \frac{d\chi}{1+z} \int_{M_{\min}}^{M_{\max}} dM \frac{dn}{dM} [f_{\nu,\text{cen}}(M, z) + f_{\nu,\text{sat}}(M, z)]. \quad (35)$$

The top panel in figure 1 shows the redshift dependence in  $I_{\nu,i}^R$  at 100 GHz and  $I_{\nu}^{\text{CIB}}$  at 217 GHz and the bottom represents the lensing kernel  $W_{\kappa}(\chi)$  for two lensing surveys of CFHTLenS (Van Waerbeke et al. 2013) and RCSLenS (Hojjati et al. 2017). In the top panel, the solid line shows the CIB intensity, while the red and blue lines are the intensity coming from BL Lac objects and steep-spectrum sources, respectively. To compute the colored lines, we assume the flux cut of  $S_{\text{lim}} = 400$  mJy at 100 GHz which is taken from Table 1 in Planck Collaboration et al. (2014d). First of all, the main contribution in CIB intensity will come from star-forming galaxies at higher redshift of  $\gtrsim 2$ , making the cross correlation with galaxy lensing irrelevant. In contrast, the radio sources can have a sizable cross correlation with large-scale structures at  $z \sim 0.2-0.4$ . Interestingly, BL Lac objects, minor population in radio flux counts at  $\sim 1$ GHz, can dominate a possible correlation with gravitational lensing in imaging survey. The model predicts BL Lac objects can be the main contributor to the mean intensity at lower redshifts ( $z < 1$ ) because of the flatness of their spectral index. We also see the impact of flux cut by comparing the red line with dashed line in the top panel in figure 1. The flux cut in the *Planck* satellite can remove the BL Lac objects at  $z \lesssim 0.1$ , but the objects at  $z \sim 0.2-0.4$  will still survive in the observed temperature maps.

Furthermore, Figure 2 represents the redshift derivative of the cross power spectrum  $d \ln C_{\kappa-T} / dz$ , showing which redshift sources the CIB or radio contamination to the tSZ-lensing signal as a function of angular scale. In this figure, the solid line shows the contri-

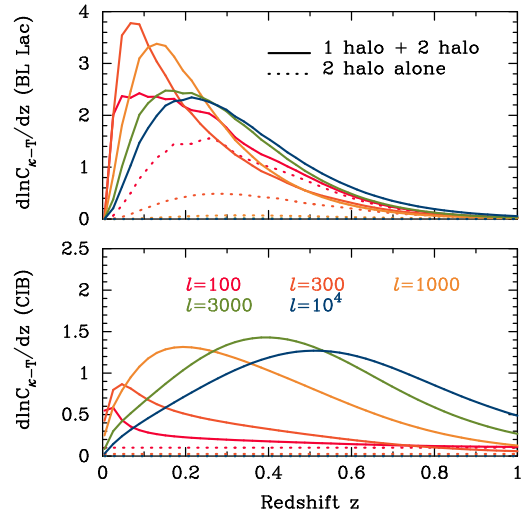


**Figure 2.** The contribution of large-scale structure at different redshifts to the cross power spectrum of weak lensing and brightness temperature. In each panel, the solid lines show the sum of one-halo and two-halo terms for a fixed multipole, while the dashed lines are for two-halo term alone. The different colored lines represent the difference in multipole  $\ell$ . In this figure, we adopt the source redshift distribution in CFHTLenS (Van Waerbeke et al. 2013). *Top:* The cumulative emission of flat-spectrum radio sources at 100 GHz. We assume the HOD parameter  $M_{\text{cut}} = 9.65 \times 10^{13} h^{-1} M_{\odot}$ . *Bottom:* The CIB intensity at 217 GHz.

bution from both of one-halo and two-halo terms, while the dashed lines are for two-halo term alone. For the radio source, we find the effective redshift to be  $0.2-0.4$  over the wide range of  $\ell = 100-10^4$  since the lensing kernel has a similar redshift dependence of the radio intensity. On the other hand, the CIB-lensing correlation would arise from large-scale structure at various redshifts, and the correlation on smaller angular scale can be determined by the structure at higher redshift.

## 5 RESULTS

### 5.1 Frequency dependence on cross correlations of astrophysical sources and lensing

The frequency dependence on the cross power spectrum  $C_{\kappa-T}$  in Eq. (8) is the key to understanding the observed tSZ-lensing correlation within our framework. Figure 3 shows the cross spectrum  $C_{\kappa-T}$  at  $\ell = 500$  as a function of frequency. Note that  $\ell = 500$  roughly corresponds to 6-7 arcmin in angular scale and it is relevant for the tension between the observed  $y - \kappa$  correlation and an expected signal from tSZ effect in ICM (Ma et al. 2015). In the top panel, solid line represents the CIB-lensing power spectrum, while dashed line is for the radio-lensing power spectrum from BL Lac objects. We here assume the HOD parameter  $M_{\text{cut}} = 9.65 \times 10^{13} h^{-1} M_{\odot}$  for BL Lac objects as same as steep-spectrum sources. In the bottom, we also plot the weight for construction of Compton  $y$  map. Black lines in the bottom correspond to the weights for extracting tSZ effect from observed temperature maps, while red line is the specific case so as to remove tSZ effects in observed Compton  $y$  map. As shown in the figure, the CIB-lensing correlation has a steep spectrum and it becomes important if high-frequency maps are weighted for  $y$ -map construction. On the other hand, the correlation with BL Lac objects and lensing convergence shows almost flat spectrum but it will be likely to dominate the cross correlation at  $\sim 100$  GHz. Since

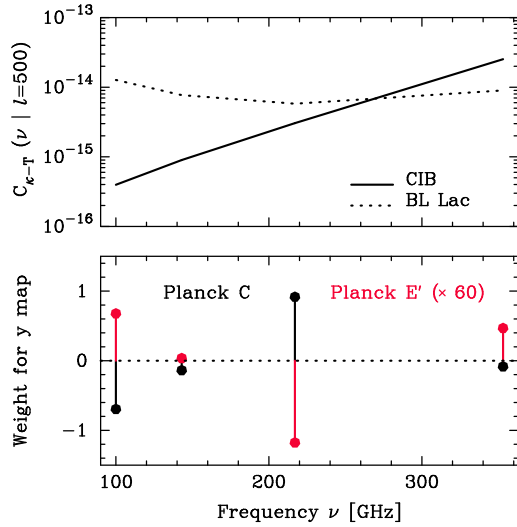


**Figure 3.** *Top:* Our model of cross power spectrum between brightness temperature in *Planck* bands and weak lensing as a function of frequency. Solid line in the top panel is the cross power spectrum between CIB and galaxy weak lensing at multipole  $\ell = 500$ , while dashed line shows the cross power spectrum between flat-spectrum radio source and lensing. We assume the source redshift distribution of galaxy lensing measurement in CFHTLenS (Van Waerbeke et al. 2014). *Bottom:* Relative contribution from multiple frequencies in construction of Compton  $y$  map. Black lines show the weight for construction of Compton  $y$  map used for measurement of tSZ-lensing correlation, while red represents the weight for evaluation of residual foreground contamination in tSZ-lensing correlation (Van Waerbeke et al. 2014).

one need a negative weight at 100 GHz with a large amplitude to obtain unbiased estimate of tSZ effect in practice (see the black line in the bottom), the radio-lensing correlation can induce a *negative* correction for observed tSZ-lensing correlation<sup>7</sup>. In addition, we expect a non-zero cross correlation arising from various terms in  $C_{\kappa-T}$  even if working with the weight to be  $\sum_i w_i g(x_i) = 0$  as in red in the bottom panel.

## 5.2 Comparison of observed tSZ-lensing cross correlation with our model

Let us then make a comparison of the observed tSZ-lensing cross correlations (Van Waerbeke et al. 2014; Hojjati et al. 2017) with our model prediction. When predicting the  $y - \kappa$  correlation in CFHTLenS, we set the gaussian filter with the beaming size of 6 arcmin for lensing convergence and the FWHM of 9.5 arcmin for Compton  $y$  map (Van Waerbeke et al. 2014). Similarly, we adopt the gaussian filter with the FWHM of 10.0 arcmin for both of  $y$  and  $\kappa$  maps in RCSLenS (Hojjati et al. 2017). Note that we apply the weight defined in CFHTLenS analyses for the RCSLenS prediction. This simplified procedure can induce a 10%-level uncertainty in theoretical model, while it is less problematic under the current statistical uncertainty (Hojjati et al. 2017).

Figure 4 summarizes the comparison with the observed correlation and our model prediction. The black points with error bar in

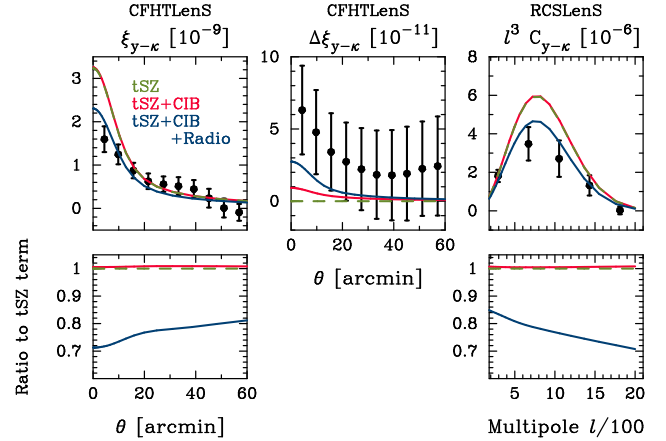


**Figure 4.** Comparison of  $y - \kappa$  correlation with recent measurements and our prediction. In the top three panels, the black points with error bar show the measurements of  $y - \kappa$  correlation in CFHTLenS (Van Waerbeke et al. 2014) and RCSLenS (Hojjati et al. 2017). Top left and right panels show the  $y - \kappa$  correlations which are expected to be dominated in tSZ-lensing correlation, while top middle panel represents the  $y - \kappa$  correlation in the absence of tSZ effects. In top panels, green dashed line shows the expected correlation from tSZ effects by ICM, red lines include the residual correlation from CIB and blue lines contain the residuals from CIB and radio sources. In the bottom panels, we show the ratio of the  $y - \kappa$  correlations with residuals from CIB and/or radio sources to the tSZ- $\kappa$  correlation expected from ICM. In this figure, we assume that the flat-spectrum radio sources live in a massive host halo with the HOD parameter of  $M_{\text{cut}} = 10^{15} h^{-1} M_{\odot}$ .

the top panels show the observed correlation taken from Van Waerbeke et al. (2014) and Hojjati et al. (2017). In the top panels, green dashed lines represent the expected correlation coming from tSZ effect in ICM (see Section 4.1), while red and blue lines include the corrections induced by the cross correlation of lensing and astrophysical sources. The red lines correspond to the signal including the CIB- $\kappa$  correlation, showing the CIB plays a minor role in observed  $y - \kappa$  correlation with weights for construction of unbiased tSZ effect (i.e. the case of  $\sum_i w_i g(x_i) = 1$ ). Including the radio sources can decrease the observed  $y - \kappa$  correlation as discussed in Section 5.1. We find that the model with  $M_{\text{cut}} = 10^{15} h^{-1} M_{\odot}$  for BL Lac objects can provide a reasonable fit to the observed  $y - \kappa$  correlation in both of CFHTLenS and RCSLenS. Note that we change single parameter of  $M_{\text{cut}}$  in the HOD of flat-spectrum radio sources by hand and keep other parameters fixed to find the model in Figure 4. This model can also explain the correlation with lensing convergence and Compton  $y$  map in the absence of tSZ effect as shown in the top middle panel. The relative correction for ICM-lensing correlation is found to be about a  $\sim 2\%$  level from CIB, while the radio sources can induce a 20–30% level correction. For a conservative scenario setting the same  $M_{\text{cut}}$  in BL Lac objects as in steep-spectrum sources, we need to take into account the correction with a level of  $\sim 10\%$  for observed  $y - \kappa$  correlation. It would be worth noting that the conservative scenario looks inconsistent with the observed  $y - \kappa$  correlation in the absence of tSZ effect, but the model with  $M_{\text{cut}} = 10^{15} h^{-1} M_{\odot}$  is in better agreement with (see Figure 5)<sup>8</sup>.

<sup>7</sup> Note that Planck Collaboration et al. (2014b,c) have also discussed similar effects; the negative response of the  $y$ -map weights to radio sources and the positive response due to dust emission.

<sup>8</sup> To place a meaningful constraint of  $M_{\text{cut}}$ , the current measurements would be insufficient due to the degeneracy among parameters in our model. To break the degeneracy among cosmology, the ICM, and residual components from CIB and faint radio sources, the tomographic tSZ-lensing correlation is expected to be essential. We will work on it in the near future.

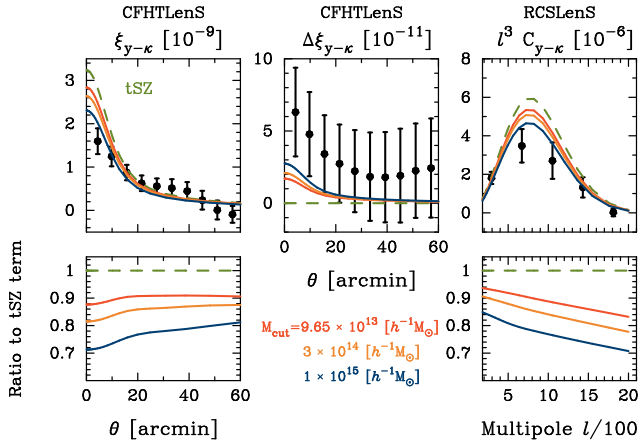


**Figure 5.** Similar to Figure 4, but this shows the dependence of the mass parameter in HOD of flat-spectrum radio sources, denoted by  $M_{\text{cut}}$ .

Can the radio sources be allowed to live in massive cluster-sized halos with masses of  $\sim 10^{15} h^{-1} M_{\odot}$  at redshift of  $z = 0.2 - 0.4$ ? This is still an open question when we think of flat-spectrum radio sources like BL Lac objects, since the measurements of clustering of radio sources have been performed at frequency of  $\sim \text{GHz}$  where steep-spectrum sources should be abundant. When adopting the model with  $M_{\text{cut}} = 10^{15} h^{-1} M_{\odot}$ , we can infer the expected halo bias of flat-spectrum sources to be  $\sim 5-8$  at  $0 < z < 1$ . This is found to be significantly higher than the halo bias of radio galaxies (e.g. Lindsay et al. 2014a,b; Nusser & Tiwari 2015; Allison et al. 2015) and radio-loud AGNs (e.g. Shen et al. 2009; Retana-Montenegro & Röttgering 2017). This finding is still in no contradiction to the existing clustering analyses of radio sources, since one can determine the halo bias of steep-spectrum sources alone from the clustering analyses in the literature.

## 6 CONCLUSION

In this paper, we studied the impact of astrophysical sources at multiple frequencies in the CMB measurement on the cross correlation between thermal Sunyaev-Zel'dovich (tSZ) effect and weak gravitational lensing effect. We developed a halo model to predict possible correlations between astrophysical sources and lensing convergence  $\kappa$ . Starting from an estimator of Compton  $y$  map in the CMB measurement, we found the correlation between astrophysical sources and lensing effect in galaxy imaging survey may affect the observed  $y - \kappa$  correlation. Assuming the best-fit model of cosmic infrared background (CIB) to the recent observation, we evaluated the CIB-lensing correlation is less important for observed  $y - \kappa$  correlation in current imaging surveys. In contrast, the radio sources with flat-spectral index of  $\sim 0.1$  can be the main contributor to the observed extragalactic intensity at  $\sim 100\text{GHz}$  and the cross correlation between such flat-spectrum sources and lensing induces a negative correction for the observed  $y - \kappa$  correlation with a level of 20-30% if the flat-spectrum sources could populate most massive dark matter halos with masses of  $\sim 10^{15} h^{-1} M_{\odot}$ . Including possible negative corrections from radio-lensing correlation enables us to explain the observed  $y - \kappa$  correlation without introducing strong AGN feedback nor a small amplitude in linear matter density fluctuations.

A caveat in our model is that the model relies on the cross correlation between lensing convergence and a minor population in radio bands. In fact, there are still large theoretical uncertainties in

the modeling of the flat-spectrum radio sources (in particular of their HOD). To improve our understanding of the observed tSZ-lensing correlation, we require additional observational tests to learn about the radio sources at  $\sim 100\text{GHz}$ . The previous measurements of clustering in radio galaxies and AGNs would not be helpful to improve our understanding of the radio-lensing correlation by flat-spectrum sources, since most of clustering measurements are subject to another population called steep-spectrum sources. We expect that the measurement of cross correlation of galaxy lensing with Compton  $y$  map in the absence of tSZ effect (i.e.  $\sum_i w_i g(x_i) = 0$  in Eq. 3) is a possible approach to determine the statistical relationship between faint flat-spectrum radio sources and dark matter halos (see also Shirasaki et al. 2018, for the study of clustering of BL Lac objects at gamma-ray frequencies). Such a measurement has large statistical uncertainty at present, whereas ongoing and future imaging surveys can change the current situation, allowing to establish a precise theoretical framework to relate flat-spectrum radio sources with large-scale structures. It would be worth noting that future studies should investigate optimal weighting of temperature maps over different frequencies to search for the relationship between radio sources and their host halos. The clustering analyses of flux-limited sample at  $\sim 100\text{GHz}$  should be a complementary approach, but the number density of flat-spectrum sources is evaluated to be of an order of  $\sim 100 \text{str}^{-1}$  with the flux cut of  $400\text{mJy}$  at  $100\text{GHz}$ . Deeper observations at  $\sim 100\text{GHz}$  will enable us to study the HOD of flat-spectrum sources in detail by increasing their number density.

It is also important for precise measurement of  $y - \kappa$  cross-correlation in the future to consider other systematic effects, for instance, the correlation between intrinsic alignment of satellite galaxies in galaxy clusters (e.g. Troxel & Ishak 2015) and the tSZ effect from the same clusters. Furthermore, it is worth exploring if lensing tomography can mitigate the impact of radio sources on observed  $y - \kappa$  correlation and developing some approach to have an unbiased estimate of tSZ-lensing correlation by fully utilizing the frequency dependence on radio-lensing correlation. We will leave those for our future studies.

## ACKNOWLEDGEMENTS

The author appreciates careful reading and suggestion to improve the article by anonymous referees. The author thanks Naoki Yoshida and J. Colin Hill for helpful comments. This work was in part supported by Grant-in-Aid for Scientific Research on Innovative Areas from the MEXT KAKENHI Grant Number (18H04358). Numerical computations presented in this paper were in part carried out on the general-purpose PC farm at Center for Computational Astrophysics, CfCA, of National Astronomical Observatory of Japan.

## APPENDIX A: HALO MODEL OF THE CROSS CORRELATION BETWEEN WEAK LENSING CONVERGENCE AND ASTROPHYSICAL SOURCES AT CMB FREQUENCIES

In this appendix, we formulate the cross correlation function between weak lensing convergence and astrophysical sources based on halo-model approach (Cooray & Sheth 2002). The lensing convergence  $\kappa$  and cumulative emission from astrophysical sources at



a given frequency  $\nu$  are expressed as

$$\kappa(\boldsymbol{\theta}) = \int d\chi W_\kappa(\chi) \delta_m(r(\chi)\boldsymbol{\theta}, z(\chi)), \quad (\text{A1})$$

$$I_\nu(\boldsymbol{\theta}) = \int d\chi W_I(\chi) j_\nu(r(\chi)\boldsymbol{\theta}, z(\chi)), \quad (\text{A2})$$

where  $I_\nu$  is the observed specific intensity,  $j_\nu$  is the comoving specific emission coefficient,  $W_I(\chi) = [1 + z(\chi)]^{-1}$ , and the kernel of  $W_\kappa$  is given by Eq. (5). Using the Limber approximation (Limber 1954), we can write the cross power spectrum between  $\kappa$  and  $I_\nu$  as

$$C_{\kappa-I}(\nu|\ell) = \int \frac{d\chi}{\chi^2} W_\kappa(\chi) W_\nu(\chi) P_{m-j\nu} \left( k = \frac{\ell}{\chi}, z(\chi) \right), \quad (\text{A3})$$

where  $P_{m-j\nu}(k, z)$  is the three-dimensional cross power spectrum between matter overdensity  $\delta_m(\mathbf{x})$  and the comoving specific emission coefficient  $j_\nu(\mathbf{x})$  at redshift of  $z$ .

In the halo model, underlying matter density field at a given redshift  $z$  can be approximated as

$$\begin{aligned} \rho_m(\mathbf{x}) &= \sum_i \rho_h(\mathbf{x} - \mathbf{x}_i | M_i, z) \\ &= \sum_i \int dM \delta_D(M - M_i) \int d^3 \mathbf{x}' \delta_D^{(3)}(\mathbf{x}' - \mathbf{x}_i) \rho_h(\mathbf{x} - \mathbf{x}' | M, z), \end{aligned} \quad (\text{A4})$$

where  $\rho_h$  is the density profile of a dark matter halo and  $\delta_D^{(n)}(\mathbf{x})$  is the  $n$ -dimensional Dirac delta function. In the following equations, we omit the redshift  $z$  for simplicity. Within the halo-model framework, the halo mass function and two-point correlation of halos are defined as

$$\left\langle \sum_i \delta_D(M - M_i) \delta_D^{(3)}(\mathbf{x} - \mathbf{x}_i) \right\rangle \equiv \frac{dn}{dM}, \quad (\text{A5})$$

$$\begin{aligned} &\left\langle \sum_{i,j|i \neq j} \delta_D(M - M_i) \delta_D^{(3)}(\mathbf{x}_1 - \mathbf{x}_i) \delta_D(M' - M_j) \delta_D^{(3)}(\mathbf{x}_2 - \mathbf{x}_j) \right\rangle \\ &= \frac{dn}{dM} \frac{dn}{dM'} \xi_{\text{hh}}(\mathbf{x}_1 - \mathbf{x}_2 | M, M'), \end{aligned} \quad (\text{A6})$$

where  $dn/dM$  is the halo mass function and  $\xi_{\text{hh}}(\mathbf{x} | M, M')$  is the halo-halo correlation function with mass of  $M$  and  $M'$ .

Similar to Eq. (A4), we can express the comoving specific emission coefficient as

$$\begin{aligned} j_\nu(\mathbf{x}) &= \sum_i \mathcal{J}_{h,\nu}(\mathbf{x} - \mathbf{x}_i | M_i) \\ &= \sum_i \int dM \delta_D(M - M_i) \int d^3 \mathbf{x}' \delta_D^{(3)}(\mathbf{x}' - \mathbf{x}_i) \mathcal{J}_{h,\nu}(\mathbf{x} - \mathbf{x}' | M), \end{aligned} \quad (\text{A7})$$

where  $\mathcal{J}_{h,\nu}$  is the emission coefficient profile in single halo and we assume it depends on halo mass  $M$ .

We then consider the three-dimensional correlation function of  $\rho_m$  and  $j_\nu$ . The correlation function is defined as

$$\bar{\rho}_m \xi_{m-j\nu}(\mathbf{x}_1 - \mathbf{x}_2) \equiv \langle \rho_m(\mathbf{x}_1) j_\nu(\mathbf{x}_2) \rangle - \bar{\rho}_m \bar{j}_\nu, \quad (\text{A8})$$

where  $\bar{\rho}_m$  is the mean matter density and  $\bar{j}_\nu$  is the spatially-averaged emission coefficient. Using Eqs. (A4)–(A7), one can decompose  $\xi_{m-j\nu}$  into two parts: one is so-called one-halo term arising from the correlation in single halos and another is two-halo term describing the correlation due to clustering of two distinct halos. The one-halo term of Eq. (A8) is given by

$$\int dM \frac{dn}{dM} \int d^3 \mathbf{y} \rho_h(\mathbf{x}_1 - \mathbf{y} | M) \mathcal{J}_{h,\nu}(\mathbf{x}_2 - \mathbf{y} | M), \quad (\text{A9})$$

while the two-halo term is

$$\begin{aligned} &\int dM \frac{dn}{dM} b(M) \int dM' \frac{dn}{dM'} b(M') \int d^3 \mathbf{y} \rho_h(\mathbf{x}_1 - \mathbf{y} | M) \\ &\quad \times \int d^3 \mathbf{y}' \mathcal{J}_{h,\nu}(\mathbf{x}_2 - \mathbf{y}' | M) \xi_L(\mathbf{y} - \mathbf{y}'), \end{aligned} \quad (\text{A10})$$

where  $b(M)$  is the linear halo bias and  $\xi_L$  is the linear matter correlation function. In Eq. (A10), we assume  $\xi_{\text{hh}}(\mathbf{x} | M, M') = b(M) b(M') \xi_L(\mathbf{x})$ . Hence, the final expression of Eq. (A8) is given by

$$\xi_{m-j\nu}(\mathbf{x}_1 - \mathbf{x}_2) = \xi_{m-j\nu}^{\text{1h}}(\mathbf{x}_1 - \mathbf{x}_2) + \xi_{m-j\nu}^{\text{2h}}(\mathbf{x}_1 - \mathbf{x}_2), \quad (\text{A11})$$

$$\xi_{m-j\nu}^{\text{1h}}(\mathbf{x}_1 - \mathbf{x}_2) = \int dM \frac{dn}{dM} \int d^3 \mathbf{y} \frac{\rho_h(\mathbf{x}_1 - \mathbf{y} | M)}{\bar{\rho}_m} \mathcal{J}_{h,\nu}(\mathbf{x}_2 - \mathbf{y} | M) \quad (\text{A12})$$

$$\begin{aligned} \xi_{m-j\nu}^{\text{2h}}(\mathbf{x}_1 - \mathbf{x}_2) &= \int dM \frac{dn}{dM} b(M) \int dM' \frac{dn}{dM'} b(M') \\ &\quad \times \int d^3 \mathbf{y} \int d^3 \mathbf{y}' \frac{\rho_h(\mathbf{x}_1 - \mathbf{y} | M)}{\bar{\rho}_m} \\ &\quad \times \mathcal{J}_{h,\nu}(\mathbf{x}_2 - \mathbf{y}' | M) \xi_L(\mathbf{y} - \mathbf{y}'). \end{aligned} \quad (\text{A13})$$

The Fourier transform of Eq. (A11) is the three-dimensional power spectrum of  $P_{m-j\nu}$ , which is expressed as

$$P_{m-j\nu}(k) = P_{m-j\nu}^{\text{1h}}(k) + P_{m-j\nu}^{\text{2h}}(k), \quad (\text{A14})$$

$$P_{m-j\nu}^{\text{1h}}(k) = \int dM \frac{dn}{dM} \frac{\bar{\rho}_h(k | M)}{\bar{\rho}_m} \tilde{\mathcal{J}}_{h,\nu}(k | M), \quad (\text{A15})$$

$$\begin{aligned} P_{m-j\nu}^{\text{2h}}(k) &= \left[ \int dM \frac{dn}{dM} b(M) \frac{\bar{\rho}_h(k | M)}{\bar{\rho}_m} \right] \\ &\quad \times \left[ \int dM' \frac{dn}{dM'} b(M') \tilde{\mathcal{J}}_{h,\nu}(k | M') \right] P_L(k), \end{aligned} \quad (\text{A16})$$

where  $P_L(k)$  is the linear matter power spectrum,  $\bar{\rho}_h$  and  $\tilde{\mathcal{J}}_{h,\nu}$  are the Fourier counterparts of  $\rho_h$  and  $\mathcal{J}_{h,\nu}$ , respectively.

To obtain the expressions in Section 4.2, we assume radio sources to be point sources and their halo occupation distribution (HOD) is expressed as an exponential form (see Eq. 23). We also assume the HOD is independent of redshift and radio luminosity. In this case, the emission coefficient profile of radio sources is given by

$$\tilde{\mathcal{J}}_\nu(k | M) = \tilde{\mathcal{J}}_{\nu,R} S(M), \quad (\text{A17})$$

$$\tilde{\mathcal{J}}_{\nu,R} = \int dL_{1.4} \frac{dn}{dL_{1.4}} \frac{L_{(1+z)\nu}(L_{1.4})}{4\pi}, \quad (\text{A18})$$

$$S(M) = \exp\left(-\frac{M_{\text{cut}}}{M}\right) \left[ \int dM' \frac{dn}{dM'} \exp\left(-\frac{M_{\text{cut}}}{M'}\right) \right]^{-1}, \quad (\text{A19})$$

where  $L_{1.4}$  is the radio luminosity at 1.4 GHz,  $dn/dL_{1.4}$  is the luminosity function, and  $L_{(1+z)\nu}(L_{1.4})$  is given by Eq. (22).

For the CIB, we adopt the model in Shang et al. (2012):

$$\tilde{\mathcal{J}}_\nu(k | M) = f_{\nu,\text{cen}}(M) + f_{\nu,\text{sat}}(M) \tilde{u}_{\text{sat}}(k | M), \quad (\text{A20})$$

where  $f_{\nu,\text{cen}}(M)$  represents the luminosity-weighted HOD of central galaxies,  $f_{\nu,\text{sat}}(M)$  is the HOD of satellites, and  $\tilde{u}_{\text{sat}}(k | M)$  is the Fourier transform of satellite number density profile. The details of luminosity-weighted HOD are found in Shang et al. (2012).

## REFERENCES

Allison R., et al., 2015, *MNRAS*, 451, 849

- Arnaud M., Pratt G. W., Piffaretti R., Böhringer H., Croston J. H., Pointecouteau E., 2010, *A&A*, **517**, A92
- Bartelmann M., Schneider P., 2001, *Physics Reports*, **340**, 291
- Battaglia N., Bond J. R., Pfrommer C., Sievers J. L., Sijacki D., 2010, *ApJ*, **725**, 91
- Battaglia N., Hill J. C., Murray N., 2015, *ApJ*, **812**, 154
- Battaglia N., Ferraro S., Schaen E., Spergel D. N., 2017, *J. Cosmology Astropart. Phys.*, **11**, 040
- Bhattacharya S., Nagai D., Shaw L., Crawford T., Holder G. P., 2012, *ApJ*, **760**, 5
- Cooray A., Sheth R., 2002, *Phys. Rep.*, **372**, 1
- Diemer B., Kravtsov A. V., 2015, *ApJ*, **799**, 108
- Dolag K., Komatsu E., Sunyaev R., 2016, *MNRAS*, **463**, 1797
- Enqvist K., Nadathur S., Sekiguchi T., Takahashi T., 2015, *J. Cosmology Astropart. Phys.*, **9**, 067
- Fixsen D. J., 2009, *ApJ*, **707**, 916
- Hill J. C., Spergel D. N., 2014, *J. Cosmology Astropart. Phys.*, **2**, 030
- Hill J. C., Baxter E. J., Lidz A., Greco J. P., Jain B., 2018, *Phys. Rev. D*, **97**, 083501
- Hojjati A., et al., 2017, *MNRAS*, **471**, 1565
- Horowitz B., Seljak U., 2017, *MNRAS*, **469**, 394
- Hu W., Kravtsov A. V., 2003, *ApJ*, **584**, 702
- Hurier G., 2015, *A&A*, **575**, L11
- Hurier G., Macías-Pérez J. F., Hildebrandt S., 2013, *A&A*, **558**, A118
- Itoh N., Kohyama Y., Nozawa S., 1998, *ApJ*, **502**, 7
- Komatsu E., Kitayama T., 1999, *ApJ*, **526**, L1
- Komatsu E., Seljak U., 2002, *MNRAS*, **336**, 1256
- Limber D. N., 1954, *ApJ*, **119**, 655
- Lindsay S. N., et al., 2014a, *MNRAS*, **440**, 1527
- Lindsay S. N., Jarvis M. J., McAlpine K., 2014b, *MNRAS*, **440**, 2322
- Ma Y.-Z., Van Waerbeke L., Hinshaw G., Hojjati A., Scott D., Zuntz J., 2015, *J. Cosmology Astropart. Phys.*, **9**, 046
- Massardi M., Bonaldi A., Negrello M., Ricciardi S., Raccanelli A., de Zotti G., 2010, *MNRAS*, **404**, 532
- Nagai D., Kravtsov A. V., Vikhlinin A., 2007, *ApJ*, **668**, 1
- Navarro J. F., Frenk C. S., White S. D. M., 1996, *ApJ*, **462**, 563
- Nozawa S., Itoh N., Kohyama Y., 1998, *ApJ*, **508**, 17
- Nusser A., Tiwari P., 2015, *ApJ*, **812**, 85
- Osato K., Flender S., Nagai D., Shirasaki M., Yoshida N., 2018, *MNRAS*, **475**, 532
- Planck Collaboration et al., 2013, *A&A*, **550**, A131
- Planck Collaboration et al., 2014a, *A&A*, **571**, A6
- Planck Collaboration et al., 2014b, *A&A*, **571**, A21
- Planck Collaboration et al., 2014c, *A&A*, **571**, A29
- Planck Collaboration et al., 2014d, *A&A*, **571**, A30
- Planck Collaboration et al., 2016a, *A&A*, **594**, A9
- Planck Collaboration et al., 2016b, *A&A*, **594**, A13
- Planck Collaboration et al., 2016c, *A&A*, **594**, A22
- Retana-Montenegro E., Röttgering H. J. A., 2017, *A&A*, **600**, A97
- Saito S., Takada M., Taruya A., 2008, *Physical Review Letters*, **100**, 191301
- Shang C., Haiman Z., Knox L., Oh S. P., 2012, *MNRAS*, **421**, 2832
- Shaw L. D., Nagai D., Bhattacharya S., Lau E. T., 2010, *ApJ*, **725**, 1452
- Shen Y., et al., 2009, *ApJ*, **697**, 1656
- Shirasaki M., Macias O., Horiuchi S., Yoshida N., Lee C.-H., Nishizawa A. J., 2018, *Phys. Rev. D*, **97**, 123015
- Smith R. E., Markovic K., 2011, *Phys. Rev. D*, **84**, 063507
- Tinker J. L., Wetzel A. R., 2010, *ApJ*, **719**, 88
- Tinker J., Kravtsov A. V., Klypin A., Abazajian K., Warren M., Yepes G., Gottlöber S., Holz D. E., 2008, *ApJ*, **688**, 709
- Tinker J. L., Robertson B. E., Kravtsov A. V., Klypin A., Warren M. S., Yepes G., Gottlöber S., 2010, *ApJ*, **724**, 878
- Troxel M. A., Ishak M., 2015, *Phys. Rep.*, **558**, 1
- Van Waerbeke L., et al., 2013, *MNRAS*, **433**, 3373
- Van Waerbeke L., Hinshaw G., Murray N., 2014, *Phys. Rev. D*, **89**, 023508
- Wake D. A., Croom S. M., Sadler E. M., Johnston H. M., 2008, *MNRAS*, **391**, 1674
- Weinberg D. H., Mortonson M. J., Eisenstein D. J., Hirata C., Riess A. G., Rozo E., 2013, *Phys. Rep.*, **530**, 87
- Zeldovich Y. B., Sunyaev R. A., 1969, *Ap&SS*, **4**, 301
- de Zotti G., Ricci R., Mesa D., Silva L., Mazzotta P., Toffolatti L., González-Nuevo J., 2005, *A&A*, **431**, 893

This paper has been typeset from a  $\text{\TeX}/\text{\LaTeX}$  file prepared by the author.